

# A finite difference method for studying thermal deformation in a double-layered thin film exposed to ultrashort pulsed lasers

Haojie Wang<sup>a</sup>, Weizhong Dai<sup>a,\*</sup>, Roderick Melnik<sup>b</sup>

<sup>a</sup> *Mathematics & Statistics, College of Engineering & Science, Louisiana Tech University, Ruston, LA 71272, USA*

<sup>b</sup> *Mathematical Modelling & Computational Sciences, Wilfrid Laurier University, Waterloo, ON, Canada N2L 3C5*

Received 31 October 2005; accepted 1 March 2006

---

## Abstract

Ultrashort pulsed lasers have been attracting worldwide interest in science and engineering because the lasers with pulse durations of order of sub-picoseconds to femtoseconds possess exclusive capabilities in limiting the undesirable spread of the thermal process zone in the heated sample. It is important to study the thermal deformation induced by ultrashort pulsed lasers to prevent thermal damage. In this article, we apply a staggered finite difference method to study thermal deformation in a two-dimensional double-layered metal film exposed to ultrashort pulsed lasers. The method is obtained based on the parabolic two-step heat transport equations. It accounts for the coupling effect between lattice temperature and strain rate, as well as for the hot-electron blast effect in momentum transfer. The developed methodology allows us to avoid non-physical oscillations in the solution as demonstrated by a series of numerical experiments.

© 2006 Elsevier Masson SAS. All rights reserved.

**Keywords:** Ultrashort-pulsed lasers; Thermal deformation; Finite difference method; Double-layered thin film; Staggered grid; Two-step model

---

## 1. Introduction

Ultrafast lasers with pulse durations of the order of sub-picoseconds to femtoseconds possess exclusive capabilities in limiting the undesirable spread of the thermal process zone in the heated sample [1]. The application of ultrashort-pulsed lasers includes structural monitoring of thin metal films [2,3], laser micromachining [4] and patterning [5], structural tailoring of microfilms [6], and laser synthesis and processing in thin-film deposition [7]. Recent applications of ultrashort-pulsed lasers have been in different disciplines such as physics, chemistry, biology, medicine, and optical technology [8–14]. The non-contact nature of femtosecond lasers has made them an ideal candidate for precise thermal processing of functional nanophase materials [1].

Success of high-energy ultrashort-pulsed lasers in real applications relies on three factors [1]:

- (1) well characterized pulse width, intensity and experimental techniques;
- (2) reliable microscale heat transfer models; and
- (3) prevention of thermal damage.

It should be pointed out here that ultrafast damage induced by sub-picosecond pulses is intrinsically different from that induced by long-pulse or continuous lasers. For the latter, laser damage is caused by elevated temperatures resulting from the continuous pumping of photon energy into the processed sample. Therefore, the “damage threshold” in heating by long-pulse lasers is often referred to as the laser intensity that drives the heated spot to the melting temperature. Thermal damage induced by ultrashort pulses in the picosecond domain, on the other hand, occurs after the heating pulse is over.

Femtosecond laser heating on metals produces a blasting force in the sub-picosecond domain, which exerts on the metal lattices along with the non-equilibrium heat flow from hot electrons. Such a hot-electron blast depends on both temperature and temperature gradient in the electron gas, resulting in pronounced effects in multi-layered metal films due to discontinuous heat transfer and load transmission across the interface.

---

\* Corresponding author.

E-mail address: [dai@coes.latech.edu](mailto:dai@coes.latech.edu) (W. Dai).

### Nomenclature

$C_{e0}$	electron heat capacity	$\text{J m}^{-3} \text{K}^{-1}$	$x_s$	optical penetration depth	m
$C_l$	lattice heat capacity	$\text{J m}^{-3} \text{K}^{-1}$	$y_s$	spatial profile parameter	m
$G$	electron-lattice coupling factor	$\text{W m}^{-3} \text{K}^{-1}$	$\alpha_T$	thermal expansion coefficient	$\text{K}^{-1}$
$J$	laser fluence	$\text{J m}^{-2}$	$\Delta t, \Delta x, \Delta y$	time increment and spatial step sizes, respectively	s, m, m
$k_e$	thermal conductivity	$\text{W m}^{-1} \text{K}^{-1}$	$\Delta_{-t}, \delta_x$	finite difference operators	
$m$	layer		$\varepsilon_x, \varepsilon_y$	normal strains in $x$ and $y$ directions, respectively	
$R$	surface reflectivity		$\Lambda$	electron-blast coefficient	$\text{J m}^{-3} \text{K}^{-2}$
$T_e$	electron temperature	K	$\gamma_{xy}$	Shear strain	
$T_l$	lattice temperature	K	$\lambda$	Lame's coefficient	Pa
$T_F$	Fermi temperature	K	$\mu$	Lame's coefficient	Pa
$t, t_n$	time	s	$\rho$	density	$\text{kg m}^{-3}$
$t_p$	laser pulse duration	s	$\sigma_x, \sigma_y$	normal stresses in $x$ and $y$ directions, respectively	Pa
$u, v$	displacements in $x$ and $y$ directions, respectively	m	$\sigma_{xy}$	Shear stress	Pa
$u_{ij}^n$	numerical solution of $u(x_i, y_j, t_n)$	m	$\phi_e$	a normalize electron temperature	
$v_1, v_2$	velocity components in $x$ and $y$ directions, respectively	$\text{m s}^{-2}$	$\phi_l$	a normalize lattice temperature	
$x, y$	Cartesian coordinates		$\chi, \eta$	material constant in electron thermal conductivity	

Up to date, as we know, only a mathematical model has been developed by Tzou and his colleagues [1] for studying thermal deformation in a double-layered thin film exposed to ultrashort pulsed lasers. They presented a one-dimensional model in a double-layered thin film. The model was solved using a differential-difference approach. In this study, we consider a two-dimensional plain strain double-layered thin film model in rectangular coordinates. The film is exposed to ultrashort pulsed lasers. An implicit finite difference scheme on a staggered grid for studying thermal deformation induced by ultrashort pulsed lasers is developed based on the parabolic two-step heat transport equations. It accounts for the coupling effect between lattice temperature and strain rate, as well as for the hot-electron blast effect in momentum transfer. The developed methodology allows us to avoid non-physical oscillations in the solution as demonstrated by a series of numerical experiments.

## 2. Mathematical model

Consider a two-dimensional double-layered thin film in rectangular coordinates, which is exposed to ultrashort pulsed lasers, as shown in Fig. 1. The governing equations for studying thermal deformation in the thin film can be expressed as follows:

(1) *Dynamic equations of motion* [1,15,16]

$$\rho^{(m)} \frac{\partial^2 u^{(m)}}{\partial t^2} = \frac{\partial \sigma_x^{(m)}}{\partial x} + \frac{\partial \sigma_{xy}^{(m)}}{\partial y} + 2\Lambda^{(m)} T_e^{(m)} \frac{\partial T_e^{(m)}}{\partial x} \quad (1)$$

$$\rho^{(m)} \frac{\partial^2 v^{(m)}}{\partial t^2} = \frac{\partial \sigma_{xy}^{(m)}}{\partial x} + \frac{\partial \sigma_y^{(m)}}{\partial y} + 2\Lambda^{(m)} T_e^{(m)} \frac{\partial T_e^{(m)}}{\partial y} \quad (2)$$

where

$$\varepsilon_x^{(m)} = \frac{\partial u^{(m)}}{\partial x}, \quad \varepsilon_y^{(m)} = \frac{\partial v^{(m)}}{\partial y}$$

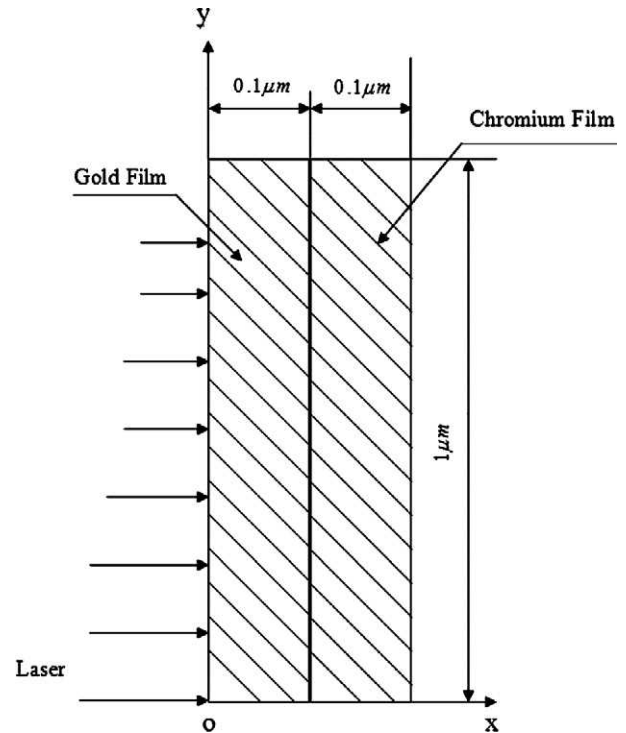


Fig. 1. Laser heating model.

$$\gamma_{xy}^{(m)} = \frac{\partial u^{(m)}}{\partial y} + \frac{\partial v^{(m)}}{\partial x} \quad (3)$$

$$\sigma_x^{(m)} = \lambda^{(m)} (\varepsilon_x^{(m)} + \varepsilon_y^{(m)}) + 2\mu^{(m)} \varepsilon_x^{(m)} - (3\lambda^{(m)} + 2\mu^{(m)}) \alpha_T^{(m)} (T_l^{(m)} - T_0) \quad (4)$$

$$\sigma_y^{(m)} = \lambda^{(m)} (\varepsilon_x^{(m)} + \varepsilon_y^{(m)}) + 2\mu^{(m)} \varepsilon_y^{(m)} - (3\lambda^{(m)} + 2\mu^{(m)}) \alpha_T^{(m)} (T_l^{(m)} - T_0) \quad (5)$$

$$\sigma_{xy}^{(m)} = \mu^{(m)} \gamma_{xy}^{(m)} \quad (6)$$

Here,  $m = 1, 2$ , denotes layer 1 and layer 2, respectively;  $u^{(m)}$  is the displacement in the thickness direction ( $x$ -direction) and  $v^{(m)}$  is the displacement in the length direction ( $y$ -direction);  $\varepsilon_x^{(m)}$  and  $\varepsilon_y^{(m)}$  are the normal strains in  $x$  and  $y$  directions, respectively;  $\gamma_{xy}^{(m)}$  is the shear strain;  $\sigma_x^{(m)}$  and  $\sigma_y^{(m)}$  are the normal stresses in  $x$  and  $y$  directions, respectively;  $\sigma_{xy}^{(m)}$  is the shear stress;  $T_e^{(m)}$  and  $T_l^{(m)}$  are electron and lattice temperatures, respectively;  $T_0$  is the initial temperature;  $\rho^{(m)}$  is density;  $\Lambda^{(m)}$  is electron–blast coefficient;  $\lambda^{(m)}$  and  $\mu^{(m)}$  are Lamé’s coefficients; and  $\alpha_T^{(m)}$  is thermal expansion coefficient.

(2) Energy equations [1,16,17,22]

$$(C_e(T_e))^{(m)} \frac{\partial T_e^{(m)}}{\partial t} = \frac{\partial}{\partial x} \left[ (k_e(T_e, T_l))^{(m)} \frac{\partial T_e^{(m)}}{\partial x} \right] + \frac{\partial}{\partial y} \left[ (k_e(T_e, T_l))^{(m)} \frac{\partial T_e^{(m)}}{\partial y} \right] - G^{(m)}(T_e^{(m)} - T_l^{(m)}) + Q \quad (7)$$

$$C_l^{(m)} \frac{\partial T_l^{(m)}}{\partial t} = G^{(m)}(T_e^{(m)} - T_l^{(m)}) - (3\lambda^{(m)} + 2\mu^{(m)})\alpha_T^{(m)} \frac{\partial}{\partial t} (\varepsilon_x^{(m)} + \varepsilon_y^{(m)}) \quad (8)$$

where the heat source is given by

$$Q = 0.94J \frac{1-R}{t_p x_s} \exp \left[ -\frac{x}{x_s} - \left( \frac{y}{y_s} \right)^2 - 2.77 \left( \frac{t-2t_p}{t_p} \right)^2 \right] \quad (9)$$

Here,  $(C_e(T_e))^{(m)} = C_{e0}^{(m)} \cdot \frac{T_e^{(m)}}{T_0}$  is the electron heat capacity;  $(k_e(T_e, T_l))^{(m)}$  is the electron thermal conductivity;  $G^{(m)}$  is the electron–lattice coupling factor;  $C_l^{(m)}$  is the lattice heat capacities;  $Q$  is energy absorption rate;  $J$  is laser fluence;  $R$  is surface reflectivity;  $t_p$  is laser pulse duration;  $x_s$  is optical penetration depth, and  $y_s$  is spatial profile parameter. Eqs. (7) and (8) are often referred to as parabolic two-step heat transport equations.

The boundary conditions are assumed to be

$$\sigma_x^{(1)} = 0, \quad \sigma_{xy}^{(1)} = 0 \quad \text{at } x = 0, \quad \text{and} \quad (10)$$

$$\sigma_x^{(2)} = 0, \quad \sigma_{xy}^{(2)} = 0 \quad \text{at } x = L_x$$

$$\sigma_y^{(1)} = 0, \quad \sigma_{xy}^{(1)} = 0 \quad \text{at } y = 0, \quad \text{and} \quad (11)$$

$$\sigma_y^{(2)} = 0, \quad \sigma_{xy}^{(2)} = 0 \quad \text{at } y = L_y$$

$$\frac{\partial T_e^{(m)}}{\partial \vec{n}} = 0, \quad \frac{\partial T_l^{(m)}}{\partial \vec{n}} = 0 \quad (12)$$

where  $\vec{n}$  is the unit outward normal vector on the boundary. It should be pointed out that insulated boundaries are imposed due to the assumption that there are no heat losses from the film surfaces in the short time response.

The interfacial conditions are assumed to be, at  $x = L_x/2$ ,

$$u^{(1)} = u^{(2)}, \quad v^{(1)} = v^{(2)} \quad (13)$$

$$\sigma_x^{(1)} = \sigma_x^{(2)}, \quad \sigma_{xy}^{(1)} = \sigma_{xy}^{(2)} \quad (14)$$

$$T_e^{(1)} = T_e^{(2)}, \quad k_e^{(1)} \frac{\partial T_e^{(1)}}{\partial x} = k_e^{(2)} \frac{\partial T_e^{(2)}}{\partial x} \quad (15)$$

The initial conditions are assumed to be

$$T_e^{(m)} = T_l^{(m)} = T_0, \quad u^{(m)} = v^{(m)} = 0$$

$$u_t^{(m)} = v_t^{(m)} = 0, \quad \text{at } t = 0 \quad (16)$$

where  $m = 1, 2$ .

### 3. Finite difference method

In order to prevent the solution from oscillations, we introduce two velocity components  $v_1^{(m)}$  and  $v_2^{(m)}$  into the model and re-write the dynamic equations of motion, Eqs. (1)–(6), as follows:

$$v_1^{(m)} = \frac{\partial u^{(m)}}{\partial t}, \quad v_2^{(m)} = \frac{\partial v^{(m)}}{\partial t} \quad (17)$$

$$\frac{\partial \varepsilon_x^{(m)}}{\partial t} = \frac{\partial v_1^{(m)}}{\partial x}, \quad \frac{\partial \varepsilon_y^{(m)}}{\partial t} = \frac{\partial v_2^{(m)}}{\partial y}$$

$$\frac{\partial \gamma_{xy}^{(m)}}{\partial t} = \frac{\partial v_2^{(m)}}{\partial x} + \frac{\partial v_1^{(m)}}{\partial y} \quad (18)$$

$$\rho^{(m)} \frac{\partial v_1^{(m)}}{\partial t} = \frac{\partial \sigma_x^{(m)}}{\partial x} + \frac{\partial \sigma_{xy}^{(m)}}{\partial y} + \Lambda^{(m)} \frac{\partial (T_e^{(m)})^2}{\partial x} \quad (19)$$

$$\rho^{(m)} \frac{\partial v_2^{(m)}}{\partial t} = \frac{\partial \sigma_{xy}^{(m)}}{\partial x} + \frac{\partial \sigma_y^{(m)}}{\partial y} + \Lambda^{(m)} \frac{\partial (T_e^{(m)})^2}{\partial y} \quad (20)$$

To develop a finite difference scheme, we first construct a staggered grid as shown in Fig. 2, where  $v_1^{(m)}$  is placed at  $(x_{i+1/2}, y_j)$ ,  $v_2^{(m)}$  is placed at  $(x_i, y_{j+1/2})$ ,  $\gamma_{xy}^{(m)}$  and  $\sigma_{xy}^{(m)}$  are placed at  $(x_{i+1/2}, y_{j+1/2})$ , while  $\varepsilon_x^{(m)}$ ,  $\varepsilon_y^{(m)}$ ,  $\sigma_x^{(m)}$ ,  $\sigma_y^{(m)}$ ,  $T_e^{(m)}$  and  $T_l^{(m)}$  are at  $(x_i, y_j)$ . Here,  $i$  and  $j$  are indices with  $1 \leq i \leq N+1$  and  $1 \leq j \leq M+1$ . We denote  $(v_1^n(i+1/2, j))^{(m)}$  and

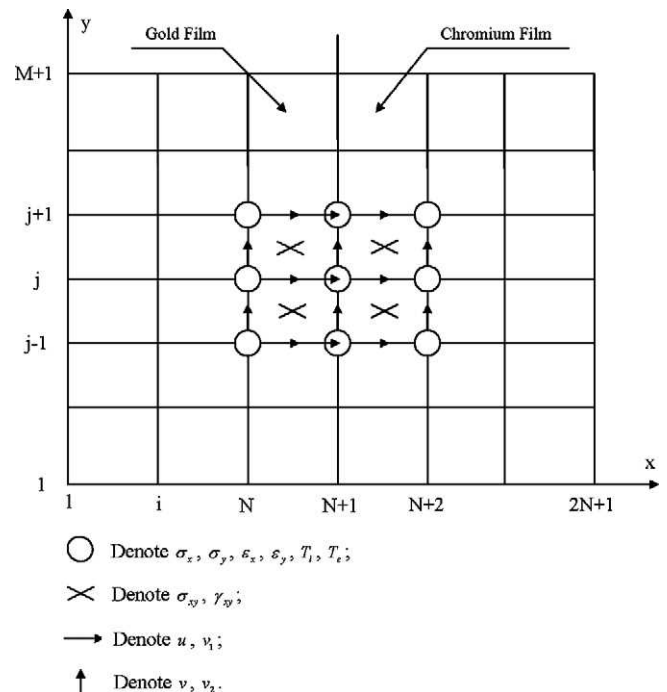


Fig. 2. A staggered mesh.

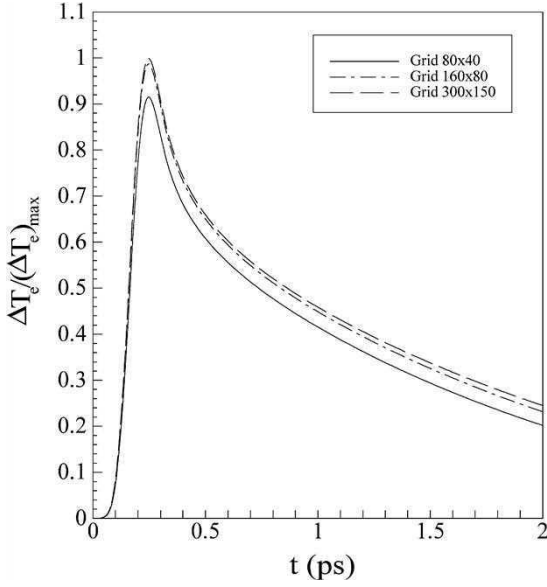


Fig. 3. Change in electron temperature at  $x = 0 \mu\text{m}$  and  $y = 0 \mu\text{m}$  versus time ( $80 \times 40$ ,  $160 \times 80$ , and  $300 \times 150$ ).

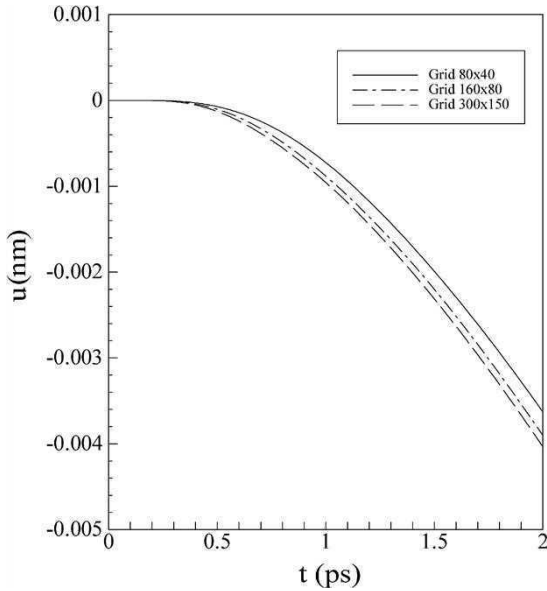


Fig. 4. Displacement ( $u$ ) at  $x = 0$  and  $y = 0$  versus time for various meshes ( $80 \times 40$ ,  $160 \times 80$ , and  $300 \times 150$ ).

$(v_2^n(i, j + 1/2))^{(m)}$  as numerical approximations of  $v_1^{(m)}((i + 1/2)\Delta x, j\Delta y, n\Delta t)$  and  $v_2^{(m)}(i\Delta x, (j + 1/2)\Delta y, n\Delta t)$ , respectively, where  $\Delta t$ ,  $\Delta x$  and  $\Delta y$  are time increment and spatial step sizes, respectively. Similar notations are used for other variables. Furthermore, we introduce the finite difference operators,  $\Delta_{-t}$  and  $\delta_x$  as follows:

$$\Delta_{-t}u^n(i, j) = u^n(i, j) - u^{n-1}(i, j)$$

$$\delta_x u^n(i, j) = u^n(i + 1/2, j) - u^n(i - 1/2, j)$$

$$\delta_y u^n(i, j) = u^n(i, j + 1/2) - u^n(i, j - 1/2)$$

We now develop a finite difference method for solving the above governing equations. To this end, we first discretize

Eqs. (19) and (20) by using an implicit finite difference scheme as follows:

$$\begin{aligned} \rho^{(m)} \frac{1}{\Delta t} \Delta_{-t} (v_1^{n+1})^{(m)}(i + 1/2, j) &= \frac{1}{\Delta x} \delta_x (\sigma_x^{n+1})^{(m)}(i + 1/2, j) \\ &+ \frac{1}{\Delta y} \delta_y (\sigma_{xy}^{n+1})^{(m)}(i + 1/2, j) \\ &+ \Lambda^{(m)} \frac{1}{\Delta x} \delta_x [(T_e^2)^{n+1}]^{(m)}(i + 1/2, j) \end{aligned} \quad (21)$$

$$\begin{aligned} \rho^{(m)} \frac{1}{\Delta t} \Delta_{-t} (v_2^{n+1})^{(m)}(i, j + 1/2) &= \frac{1}{\Delta x} \delta_x (\sigma_{xy}^{n+1})^{(m)}(i, j + 1/2) \\ &+ \frac{1}{\Delta y} \delta_y (\sigma_y^{n+1})^{(m)}(i, j + 1/2) \\ &+ \Lambda^{(m)} \frac{1}{\Delta y} \delta_y [(T_e^2)^{n+1}]^{(m)}(i, j + 1/2) \end{aligned} \quad (22)$$

where Eq. (18) and Eqs. (4), (5), (6) are discretized as,

$$\frac{1}{\Delta t} \Delta_{-t} (\varepsilon_x^{n+1})^{(m)}(i, j) = \frac{1}{\Delta x} \delta_x (v_1^{n+1})^{(m)}(i, j) \quad (23a)$$

$$\frac{1}{\Delta t} \Delta_{-t} (\varepsilon_y^{n+1})^{(m)}(i, j) = \frac{1}{\Delta y} \delta_y (v_2^{n+1})^{(m)}(i, j) \quad (23b)$$

$$\begin{aligned} \frac{1}{\Delta t} \Delta_{-t} (\gamma_{xy}^{n+1})^{(m)}(i + 1/2, j + 1/2) &= \frac{1}{\Delta x} \delta_x (v_2^{n+1})^{(m)}(i + 1/2, j + 1/2) \\ &+ \frac{1}{\Delta y} \delta_y (v_1^{n+1})^{(m)}(i + 1/2, j + 1/2) \end{aligned} \quad (23c)$$

$$\begin{aligned} (\sigma_x^{n+1})^{(m)}(i, j) &= \lambda^{(m)} [(\varepsilon_x^{n+1})^{(m)}(i, j) + (\varepsilon_y^{n+1})^{(m)}(i, j)] \\ &+ 2\mu^{(m)} (\varepsilon_x^{n+1})^{(m)}(i, j) \\ &- (3\lambda^{(m)} + 2\mu^{(m)}) \alpha_T^{(m)} [(T_l^{n+1})^{(m)}(i, j) - T_0] \end{aligned} \quad (24)$$

$$\begin{aligned} (\sigma_y^{n+1})^{(m)}(i, j) &= \lambda^{(m)} [(\varepsilon_x^{n+1})^{(m)}(i, j) + (\varepsilon_y^{n+1})^{(m)}(i, j)] \\ &+ 2\mu^{(m)} (\varepsilon_y^{n+1})^{(m)}(i, j) \\ &- (3\lambda^{(m)} + 2\mu^{(m)}) \alpha_T^{(m)} [(T_l^{n+1})^{(m)}(i, j) - T_0] \end{aligned} \quad (25)$$

$$\begin{aligned} (\sigma_{xy}^{n+1})^{(m)}(i + 1/2, j + 1/2) &= \mu^{(m)} [(\gamma_{xy}^{n+1})^{(m)}(i + 1/2, j + 1/2)] \end{aligned} \quad (26)$$

We then discretize Eqs. (7) and (8) using the Crank–Nicholson method as follows:

$$\begin{aligned} C_{e0}^{(m)} \frac{(T_e^{n+1})^{(m)}(i, j) + (T_e^n)^{(m)}(i, j)}{2} \cdot \frac{1}{\Delta t} \Delta_{-t} (T_e^{n+1})^{(m)}(i, j) &= \frac{1}{2\Delta x^2} [(k_e^{n+1})^{(m)}(i + 1/2, j) \delta_x (T_e^{n+1})^{(m)}(i + 1/2, j) \\ &- (k_e^{n+1})^{(m)}(i - 1/2, j) \delta_x (T_e^{n+1})^{(m)}(i - 1/2, j)] \end{aligned}$$

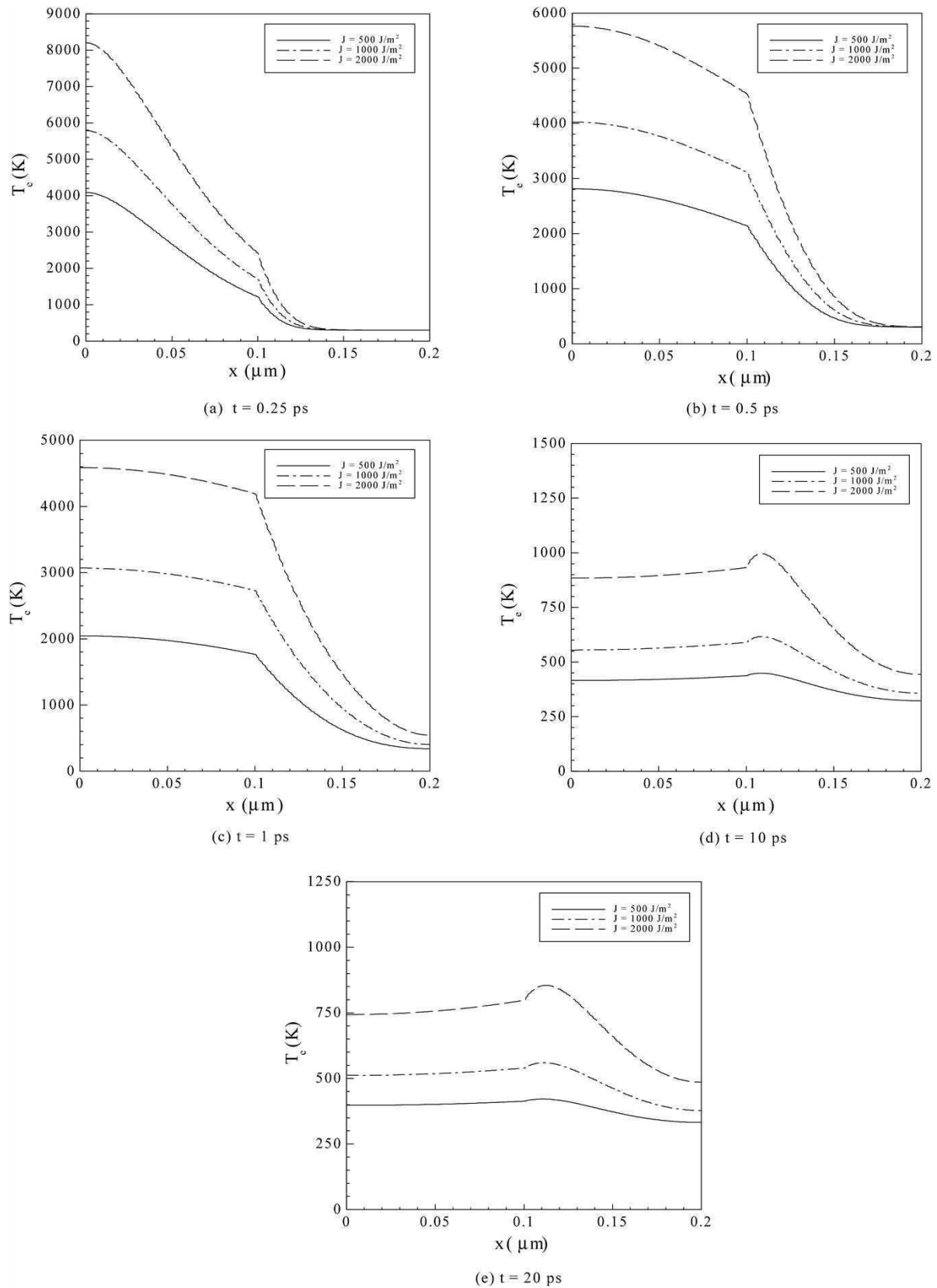


Fig. 5. Comparison of electron temperature at  $y = 0 \mu\text{m}$  at different times with three different laser fluences.

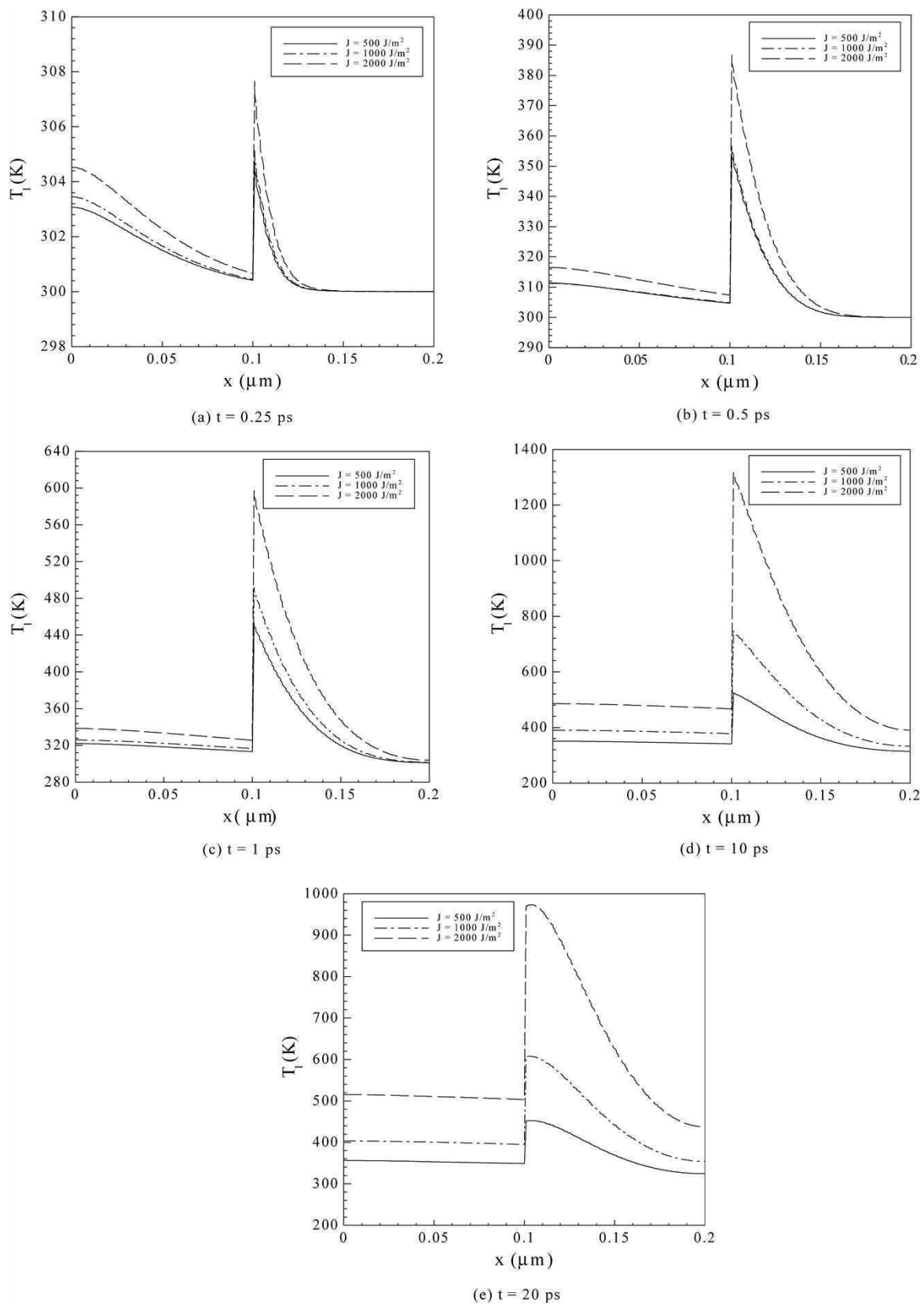


Fig. 6. Comparison of lattice temperature at  $y = 0 \mu\text{m}$  at different times with three different laser fluences.

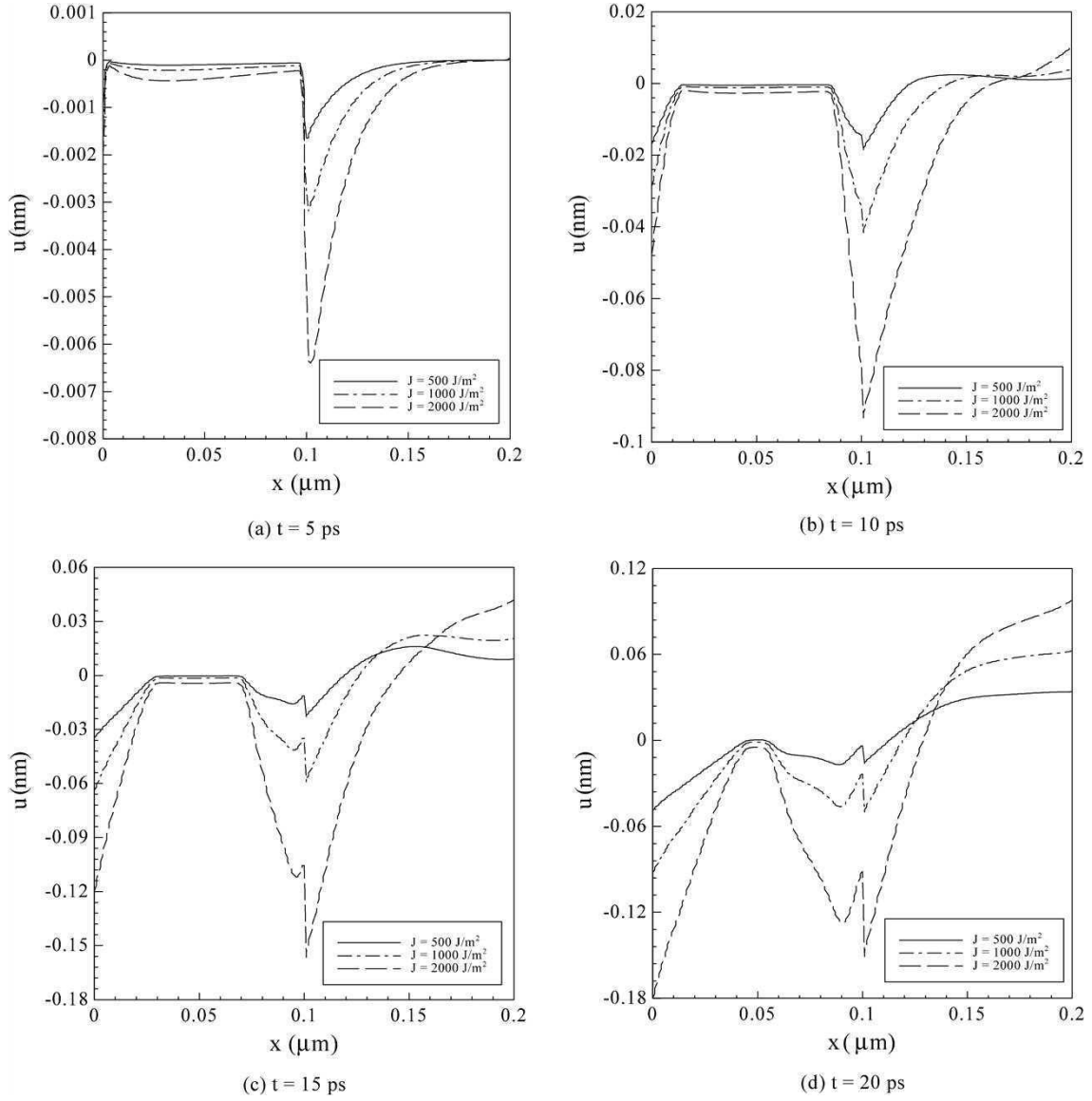


Fig. 7. Comparison of displacement ( $u$ ) at  $y = 0 \mu\text{m}$  at different times with three different laser fluences.

$$\begin{aligned}
 & + \frac{1}{2\Delta x^2} [(k_e^n)^{(m)}(i+1/2, j) \delta_x (T_e^n)^{(m)}(i+1/2, j) \\
 & - (k_e^n)^{(m)}(i-1/2, j) \delta_x (T_e^n)^{(m)}(i-1/2, j)] \\
 & + \frac{1}{2\Delta y^2} [(k_e^{n+1})^{(m)}(i, j+1/2) \delta_x (T_e^{n+1})^{(m)}(i, j+1/2) \\
 & - (k_e^{n+1})^{(m)}(i, j-1/2) \delta_x (T_e^{n+1})^{(m)}(i, j-1/2)] \\
 & + \frac{1}{2\Delta y^2} [(k_e^n)^{(m)}(i, j+1/2) \delta_x (T_e^n)^{(m)}(i, j+1/2) \\
 & - (k_e^n)^{(m)}(i, j-1/2) \delta_x (T_e^n)^{(m)}(i, j-1/2)] \\
 & - G^{(m)} \left[ \frac{(T_e^{n+1})^{(m)}(i, j) + (T_e^n)^{(m)}(i, j)}{2} \right. \\
 & \left. - \frac{(T_l^{n+1})^{(m)}(i, j) + (T_l^n)^{(m)}(i, j)}{2} \right] \\
 & + Q^{n+1/2}(i, j)
 \end{aligned} \tag{27}$$

and

$$\begin{aligned}
 & C_l^{(m)} \frac{1}{\Delta t} \Delta_{-t} (T_l^{n+1})^{(m)}(i, j) \\
 & = G^{(m)} \left[ \frac{(T_e^{n+1})^{(m)}(i, j) + (T_e^n)^{(m)}(i, j)}{2} \right. \\
 & \quad \left. - \frac{(T_l^{n+1})^{(m)}(i, j) + (T_l^n)^{(m)}(i, j)}{2} \right] \\
 & \quad - (3\lambda^{(m)} + 2\mu^{(m)}) \alpha_T^{(m)} \left[ \frac{\Delta_{-t} (\varepsilon_x^{n+1})^{(m)}(i, j)}{\Delta t} \right. \\
 & \quad \left. + \frac{\Delta_{-t} (\varepsilon_y^n)^{(m)}(i, j)}{\Delta t} \right]
 \end{aligned} \tag{28}$$

Finally, the displacements,  $u^{(m)}$  and  $v^{(m)}$ , are obtained using the Euler backward scheme for Eq. (17) as follows:

$$\frac{1}{\Delta t} \Delta_{-t} (u^{n+1})^{(m)}(i+1/2, j) = (v_1^{n+1})^{(m)}(i+1/2, j) \tag{29a}$$

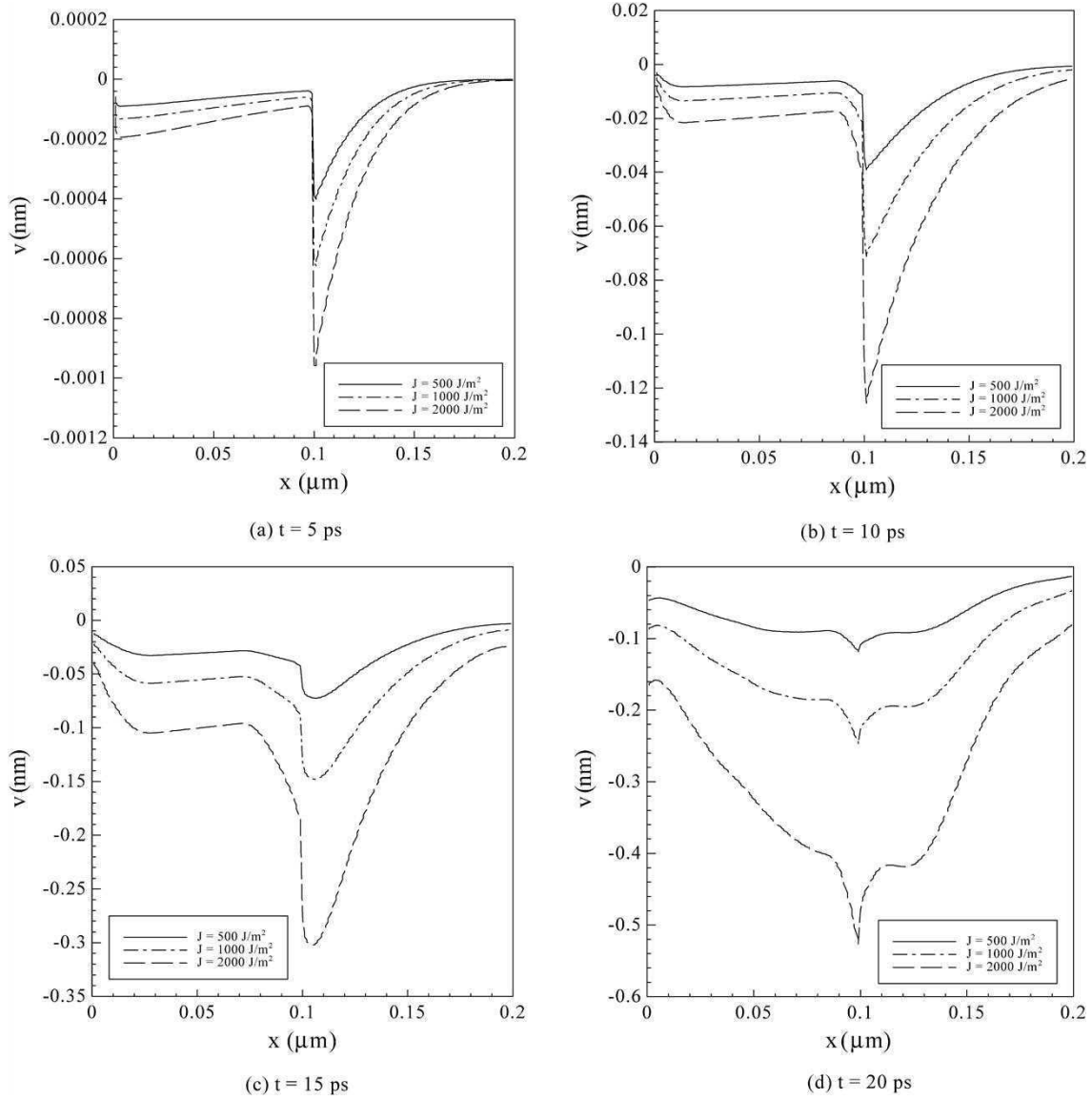


Fig. 8. Comparison of displacement ( $v$ ) at  $y = 0 \mu\text{m}$  at different times with three different laser fluences.

$$\frac{1}{\Delta t} \Delta_{-t} (v^{n+1})^{(m)}(i, j + 1/2) = (v_2^{n+1})^{(m)}(i, j + 1/2) \quad (29b)$$

The boundary conditions, Eqs. (10)–(12), are discretized as follows:

$$\begin{aligned} (\sigma_x^{n+1})^{(1)}(1, j) &= 0, & (\sigma_x^{n+1})^{(2)}(N+1, j) &= 0 \\ (\sigma_{xy}^{n+1})^{(1)}(1, j) &= 0, & (\sigma_{xy}^{n+1})^{(2)}(N+1, j) &= 0, \\ 1 \leq j \leq M+1 \end{aligned} \quad (30)$$

$$\begin{aligned} (\sigma_y^{n+1})^{(1)}(i, 1) &= 0, & (\sigma_y^{n+1})^{(2)}(i, M+1) &= 0, \\ (\sigma_{xy}^{n+1})^{(1)}(i, 1) &= 0, & (\sigma_{xy}^{n+1})^{(2)}(i, M+1) &= 0, \\ 1 \leq i \leq N+1 \end{aligned} \quad (31)$$

$$\begin{aligned} (T_e^{n+1})^{(1)}(1, j) &= (T_e^{n+1})^{(1)}(2, j) \\ (T_e^{n+1})^{(2)}(N+1, j) &= (T_e^{n+1})^{(2)}(N, j) \\ 1 \leq j \leq M+1 \end{aligned} \quad (32a)$$

$$\begin{aligned} (T_e^{n+1})^{(m)}(i, 1) &= (T_e^{n+1})^{(m)}(i, 2) \\ (T_e^{n+1})^{(m)}(i, M+1) &= (T_e^{n+1})^{(m)}(i, M) \\ 1 \leq i \leq N+1 \end{aligned} \quad (32b)$$

$$\begin{aligned} (T_l^{n+1})^{(1)}(1, j) &= (T_l^{n+1})^{(1)}(2, j) \\ (T_l^{n+1})^{(2)}(N+1, j) &= (T_l^{n+1})^{(2)}(N, j) \\ 1 \leq j \leq M+1 \end{aligned} \quad (33a)$$

$$\begin{aligned} (T_l^{n+1})^{(m)}(i, 1) &= (T_l^{n+1})^{(m)}(i, 2) \\ (T_l^{n+1})^{(m)}(i, M+1) &= (T_l^{n+1})^{(m)}(i, M) \\ 1 \leq i \leq N+1 \end{aligned} \quad (33b)$$

for any time level  $n$  and  $m = 1, 2$ .

The interfacial conditions in Eqs. (13)–(15) are employed and then discretized in this way. First, the interfacial condition



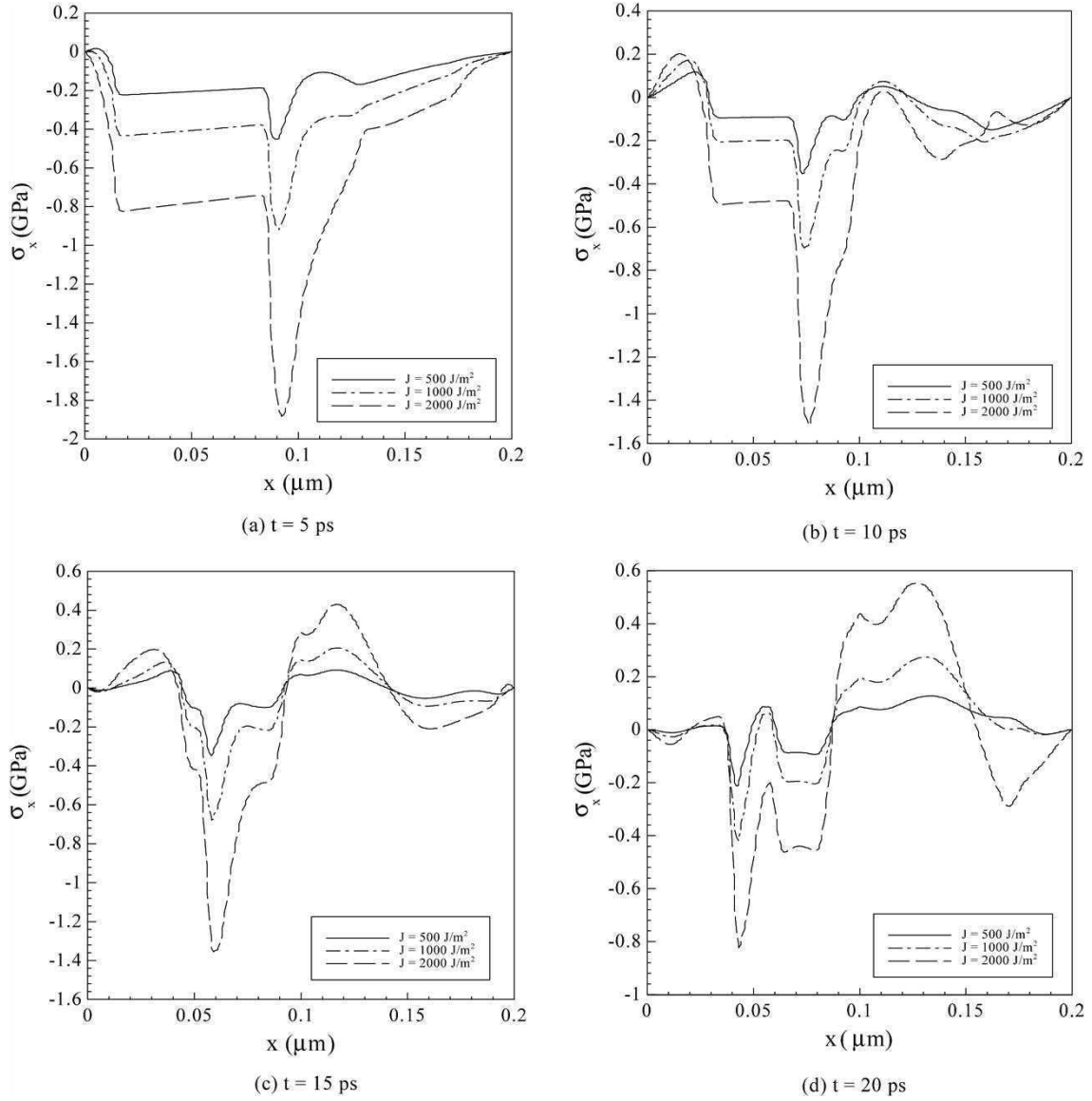


Fig. 9. Comparison of normal stress ( $\sigma_x$ ) at  $y = 0 \mu\text{m}$  at different times with three different laser fluences.

for velocity components  $v_1^{(m)}$  and  $v_2^{(m)}$  based on Eq. (13) can be written as  $v_1^{(1)} = v_1^{(2)}$  and  $v_2^{(1)} = v_2^{(2)}$ . Hence, we assume that

$$(v_1^{n+1})^{(1)}(N+1, j) = (v_1^{n+1})^{(2)}(1, j) \quad (34a)$$

$$(v_2^{n+1})^{(1)}(N+1, j) = (v_2^{n+1})^{(2)}(1, j) \quad (34b)$$

Second, Eq. (15) is discretized as follows:

$$k_e^{(1)} \frac{(T_e^{n+1})^{(1)}(N+1, j) - (T_e^{n+1})^{(1)}(N, j)}{\Delta x} = k_e^{(2)} \frac{(T_e^{n+1})^{(2)}(2, j) - (T_e^{n+1})^{(2)}(1, j)}{\Delta x} \quad (35a)$$

$$(T_e^{n+1})^{(1)}(N+1, j) = (T_e^{n+1})^{(2)}(1, j) \quad (35b)$$

Third, coupled with Eqs. (4)–(6), Eq. (14) is discretized as

$$(\lambda^{(1)} + 2\mu^{(1)})(\varepsilon_x^{n+1})^{(1)}(N+1, j) + \lambda^{(1)}(\varepsilon_y^{n+1})^{(1)}(N+1, j) - (3\lambda^{(1)} + 2\mu^{(1)})\alpha_T^{(1)}[(T_l^{n+1})^{(1)}(N+1, j) - T_0]$$

$$= (\lambda^{(2)} + 2\mu^{(2)})(\varepsilon_x^{n+1})^{(2)}(N+1, j) + \lambda^{(2)}(\varepsilon_y^{n+1})^{(2)}(N+1, j) - (3\lambda^{(2)} + 2\mu^{(2)})\alpha_T^{(2)}[(T_l^{n+1})^{(2)}(N+1, j) - T_0] \quad (36a)$$

$$\mu^{(1)}(\gamma_{xy}^{n+1})^{(1)}(N+1, j) = \mu^{(2)}(\gamma_{xy}^{n+1})^{(2)}(1, j) \quad (36b)$$

where  $(\varepsilon_x^{n+1})^{(1)}(N+1, j)$ ,  $(\varepsilon_x^{n+1})^{(2)}(1, j)$ ,  $(\varepsilon_y^{n+1})^{(1)}(N+1, j)$ ,  $(\varepsilon_y^{n+1})^{(2)}(1, j)$ ,  $(\gamma_{xy}^{n+1})^{(1)}(N+1, j)$ , and  $(\gamma_{xy}^{n+1})^{(2)}(1, j)$  are obtained based on Eqs. (23a)–(23c) as follows:

$$(\varepsilon_x^{n+1})^{(1)}(N+1, j) = \frac{(v_1^{n+1})^{(1)}(N+1, j) - (v_1^{n+1})^{(1)}(N, j)}{\Delta x/2} \Delta t + (\varepsilon_x^n)^{(1)}(N+1, j) \quad (37a)$$

$$(\varepsilon_x^{n+1})^{(2)}(1, j) = \frac{(v_1)^{(2)}(2, j) - (v_1)^{(2)}(1, j)}{\Delta x/2} \Delta t + (\varepsilon_x^n)^{(2)}(1, j) \quad (37b)$$

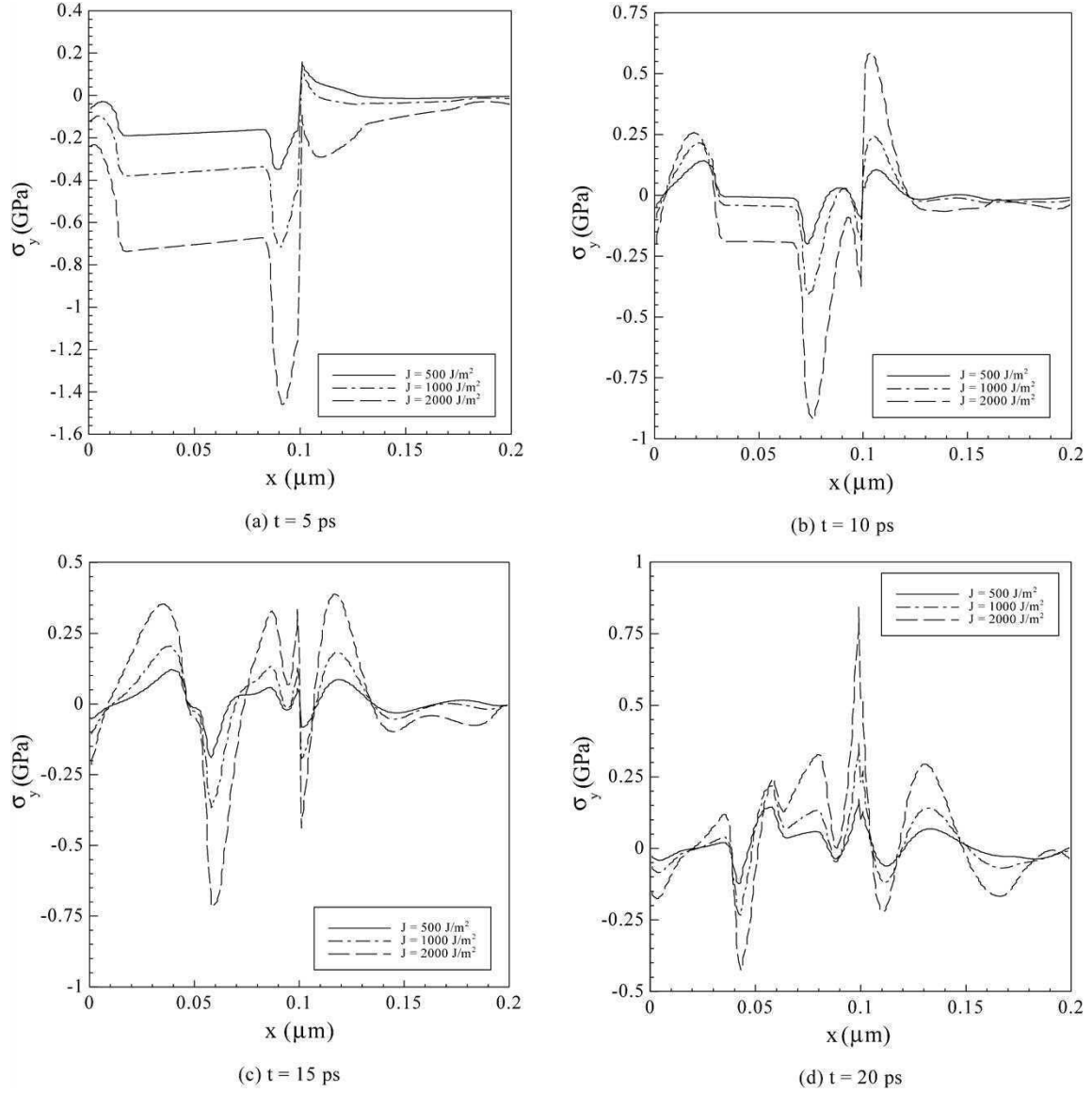


Fig. 10. Comparison of normal stress ( $\sigma_y$ ) at  $y = 0 \mu\text{m}$  at different times with three different laser fluences.

$$\begin{aligned}
 & (\varepsilon_y^{n+1})^{(1)}(N+1, j) \\
 &= \frac{(v_2)^{(1)}(N+1, j) - (v_2)^{(1)}(N+1, j-1)}{\Delta y} \Delta t \\
 &+ (\varepsilon_y^n)^{(1)}(N+1, j)
 \end{aligned} \quad (38a)$$

$$\begin{aligned}
 & (\varepsilon_y^{n+1})^{(2)}(1, j) \\
 &= \frac{(v_2)^{(2)}(2, j) - (v_2)^{(2)}(1, j-1)}{\Delta y} \Delta t + (\varepsilon_y^n)^{(2)}(1, j)
 \end{aligned} \quad (38b)$$

$$\begin{aligned}
 & (\gamma_{xy}^{n+1})^{(1)}(N+1, j) \\
 &= \frac{\Delta t}{\Delta y} [(v_1^{n+1})^{(1)}(N+1, j+1) - (v_1^{n+1})^{(1)}(N+1, j)] \\
 &+ \frac{\Delta t}{\Delta x} [(v_2^{n+1})^{(1)}(N+1, j) - (v_2^{n+1})^{(1)}(N, j)] \\
 &+ (\gamma_{xy}^n)^{(1)}(N+1, j)
 \end{aligned} \quad (39a)$$

$$\begin{aligned}
 & (\gamma_{xy}^{n+1})^{(2)}(1, j) \\
 &= \frac{\Delta t}{\Delta y} [(v_1^{n+1})^{(2)}(1, j+1) - (v_1^{n+1})^{(2)}(1, j)] \\
 &+ \frac{\Delta t}{\Delta x} [(v_2^{n+1})^{(2)}(2, j) - (v_2^{n+1})^{(2)}(1, j)] \\
 &+ (\gamma_{xy}^n)^{(2)}(1, j)
 \end{aligned} \quad (39b)$$

where  $1 \leq j \leq M+1$  and  $m = 1, 2$ .

Finally, the initial conditions, Eq. (16), are approximated as

$$(u^0)^{(m)}(i+1/2, j) = 0, \quad (v^0)^{(m)}(i, j+1/2) = 0 \quad (40a)$$

$$(v_1^0)^{(m)}(i+1/2, j) = 0, \quad (v_1^0)^{(m)}(i, j+1/2) = 0 \quad (40b)$$

$$(T_e^0)^{(m)}(i, j) = T_0, \quad (T_l^0)^{(m)}(i, j) = T_0 \quad (40c)$$

It can be seen that the truncation error of Eqs. (21)–(23) is  $O(\Delta t + \Delta x^2 + \Delta y^2)$  and the truncation error of Eqs. (27)

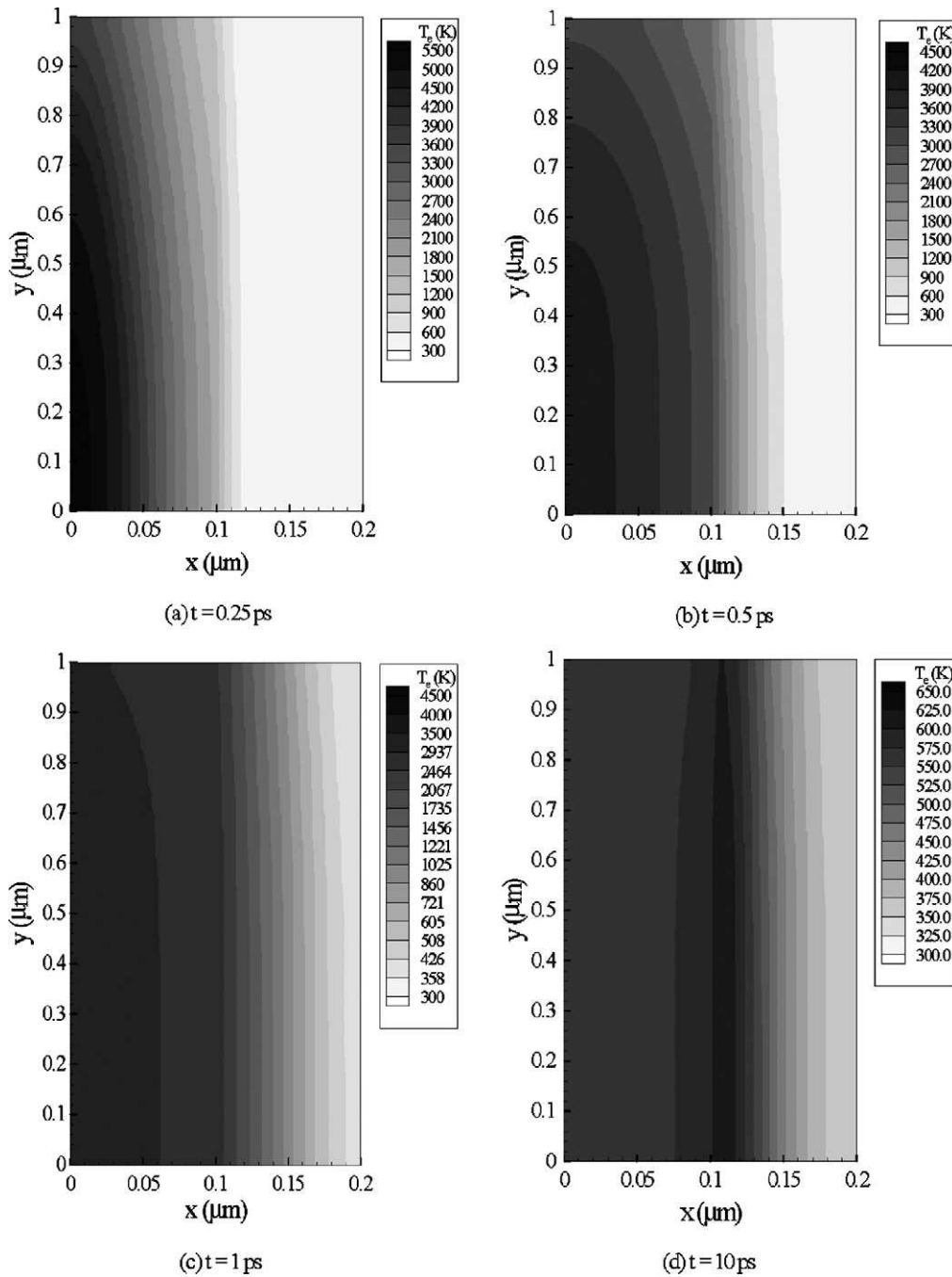


Fig. 11. Electron temperature (K) profiles at different times with laser fluence  $J = 1000 \text{ J m}^{-2}$ .

and (28) is  $O(\Delta t^2 + \Delta x^2 + \Delta y^2)$ . It should be pointed out that Eqs. (21) and (22) are nonlinear since the terms  $\delta_x[(T_e^2)^{n+1}]^{(m)}(i + 1/2, j)$  and  $\delta_x[(T_e^2)^{n+1}]^{(m)}(i, j + 1/2)$  are nonlinear. Also, it can be seen that Eqs. (27) and (28) are nonlinear. Therefore, the above scheme must be solved iteratively. An iterative algorithm for solving the above scheme, Eqs. (21)–(40), at time level  $n + 1$  can be described as follows:

**Step 1.** Guess  $(\epsilon_x^{n+1})^{(m)}$ ,  $(\epsilon_y^{n+1})^{(m)}$ , and  $(\gamma_{xy}^{n+1})^{(m)}$ , and solve Eqs. (27) and (28) iteratively for  $(T_e^{n+1})^{(m)}$  and  $(T_l^{n+1})^{(m)}$ .

- Step 2.** Solve for  $(\sigma_x^{n+1})^{(m)}$ ,  $(\sigma_y^{n+1})^{(m)}$ , and  $(\sigma_{xy}^{n+1})^{(m)}$  using Eqs. (24)–(26).
- Step 3.** Solve for  $(v_1^{n+1})^{(m)}$  and  $(v_2^{n+1})^{(m)}$  using Eqs. (21) and (22).
- Step 4.** Update  $(\epsilon_x^{n+1})^{(m)}$ ,  $(\epsilon_y^{n+1})^{(m)}$  and  $(\gamma_{xy}^{n+1})^{(m)}$  using Eq. (23).
- Step 5.** Repeat the above steps until a convergent solution is obtained, and then solve for  $(u^{n+1})^{(m)}$  and  $(v^{n+1})^{(m)}$  using Eq. (29).

It should be pointed out that the interface is computed in this way: we first obtain updated  $(T_e^{n+1})^{(1)}(N + 1, j)$  and

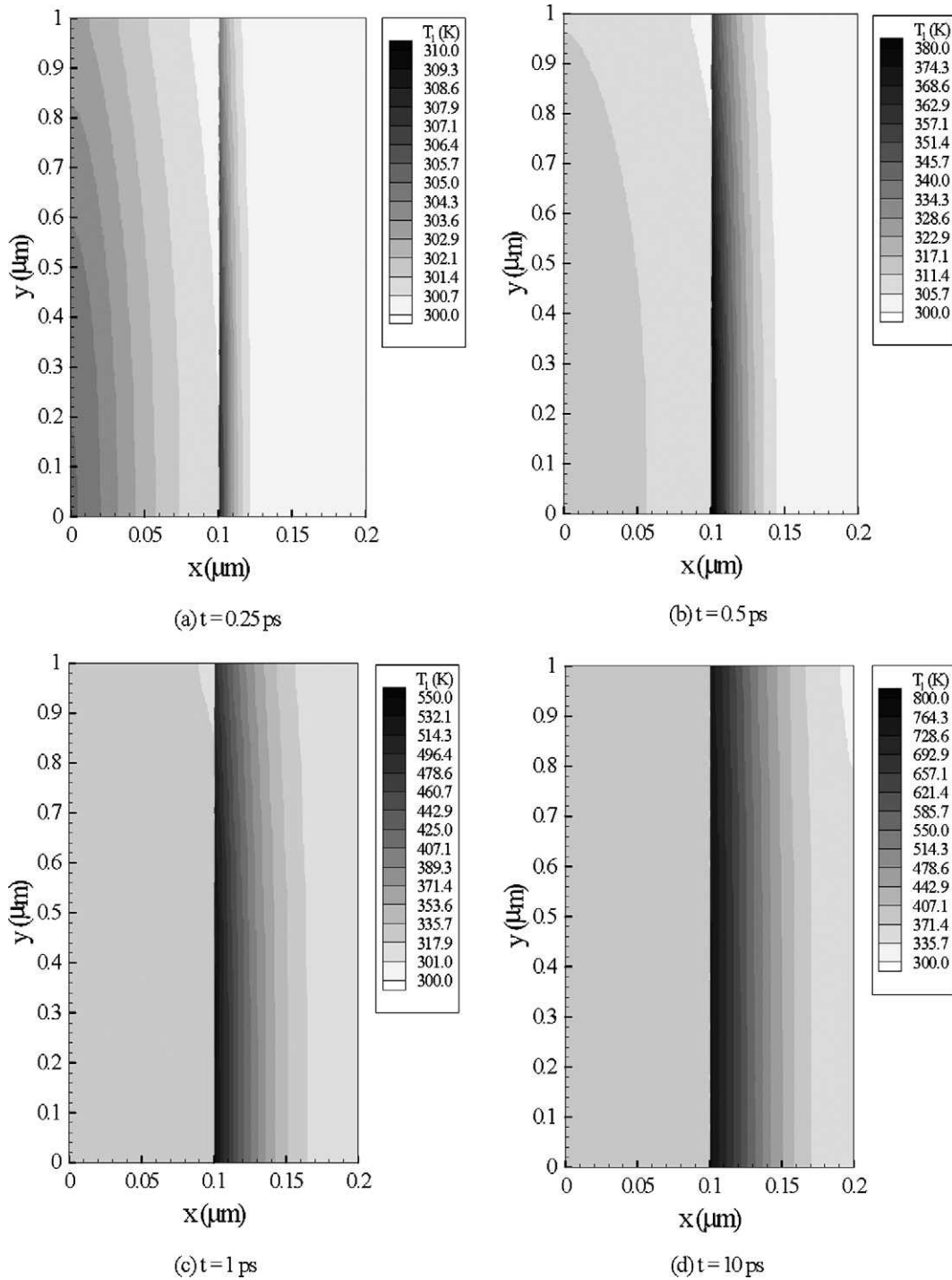


Fig. 12. Lattice temperature (K) profiles at different times with laser fluence  $J = 1000 \text{ J m}^{-2}$ .

$(T_e^{n+1})^{(2)}(1, j)$  from Eq. (35), and substitute them into Eq. (28) to obtain updated  $(T_l^{n+1})^{(1)}(N+1, j)$  and  $(T_l^{n+1})^{(2)}(1, j)$ ; we then substitute Eqs. (34), (37), and (38) into Eq. (36a) to obtain updated  $(v_1^{n+1})^{(1)}(N+1, j)$  and  $(v_1^{n+1})^{(2)}(1, j)$ ; we further substitute Eqs. (34) and (39) into Eq. (36b) to obtain updated  $(v_2^{n+1})^{(1)}(N+1, j)$  and  $(v_2^{n+1})^{(2)}(1, j)$ ; and from the above known variables on the interface nodes we can obtain  $(\varepsilon_x^{n+1})^{(m)}$ ,  $(\varepsilon_y^{n+1})^{(m)}$ ,  $(\gamma_{xy}^{n+1})^{(m)}$ ,  $(\sigma_x^{n+1})^{(m)}$ ,  $(\sigma_y^{n+1})^{(m)}$ ,  $(\sigma_{xy}^{n+1})^{(m)}$ ,  $(u^{n+1})^{(m)}$  and  $(v^{n+1})^{(m)}$  on the interface nodes

using Eqs. (37)–(39), Eqs. (24)–(26), and Eq. (29), respectively.

#### 4. Numerical examples

To test the applicability of the developed numerical scheme, Eqs. (21)–(40), we investigated the temperature rise and deformation in a double-layered thin film consisting of a gold layer padding on a chromium layer with the dimensions  $0.1 \mu\text{m}$  (thickness)  $\times 1 \mu\text{m}$  (length) each layer, as shown in Fig. 1. The

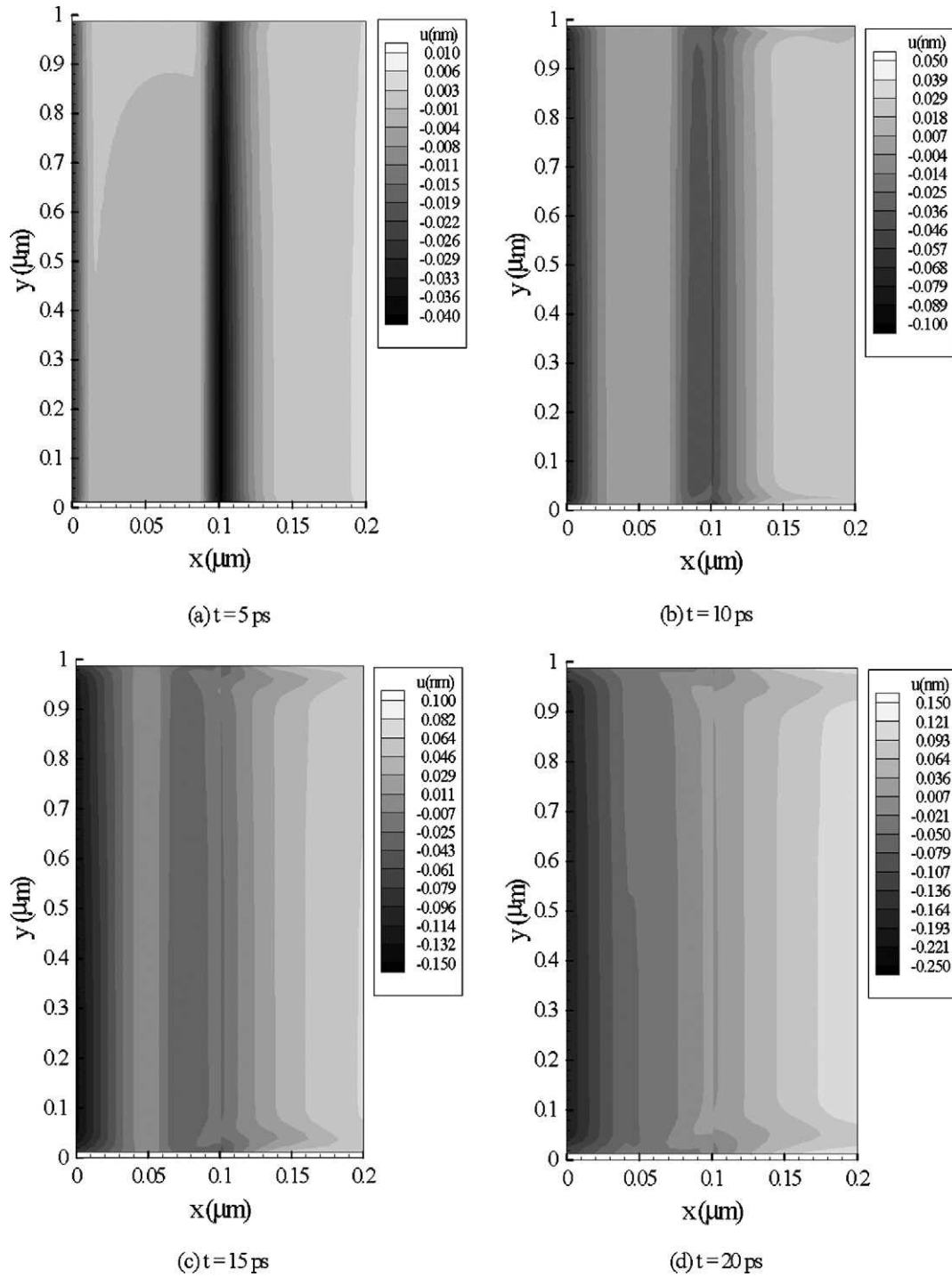


Fig. 13. Displacement ( $u$ ) profiles at different times with laser fluence  $J = 1000 \text{ J m}^{-2}$ .

electron thermal conductivity  $((k_e(T_e, T_l))^{(m)})$  was chosen to be [1,16,17]

$$(k_e(T_e, T_l))^{(m)} = k_{e0}^{(m)} \cdot \frac{T_e^{(m)}}{T_l^{(m)}} \quad (41)$$

The thermophysical properties for gold and chromium are listed in Table 1 [18,19]. Three meshes of  $80 \times 40$ ,  $160 \times 80$ ,  $300 \times 150$  were chosen in order to test the convergence of the scheme. The time increment is to be 0.005 ps.  $T_0$  was set to

be 300 K. Three different values of laser fluences ( $J = 500 \text{ J m}^{-2}$ ,  $1000 \text{ J m}^{-2}$  and  $2000 \text{ J m}^{-2}$ ) were chosen to study the hot-electron blast force.

Fig. 3 shows the change in electron temperature  $(\Delta T_e / (\Delta T_e)_{\max})$  at  $x = 0$  and  $y = 0$  with laser fluence  $J = 500 \text{ J m}^{-2}$ . The maximum temperature rise of  $T_e^{(1)}$  (i.e.,  $(\Delta T_e)_{\max}$ ) is about 3790 K, which is very close to that obtained by Qiu and Tien [20]. Fig. 4 shows the displacement ( $u$ ) at  $x = 0$  and  $y = 0$  versus time. It can be seen from both figures that

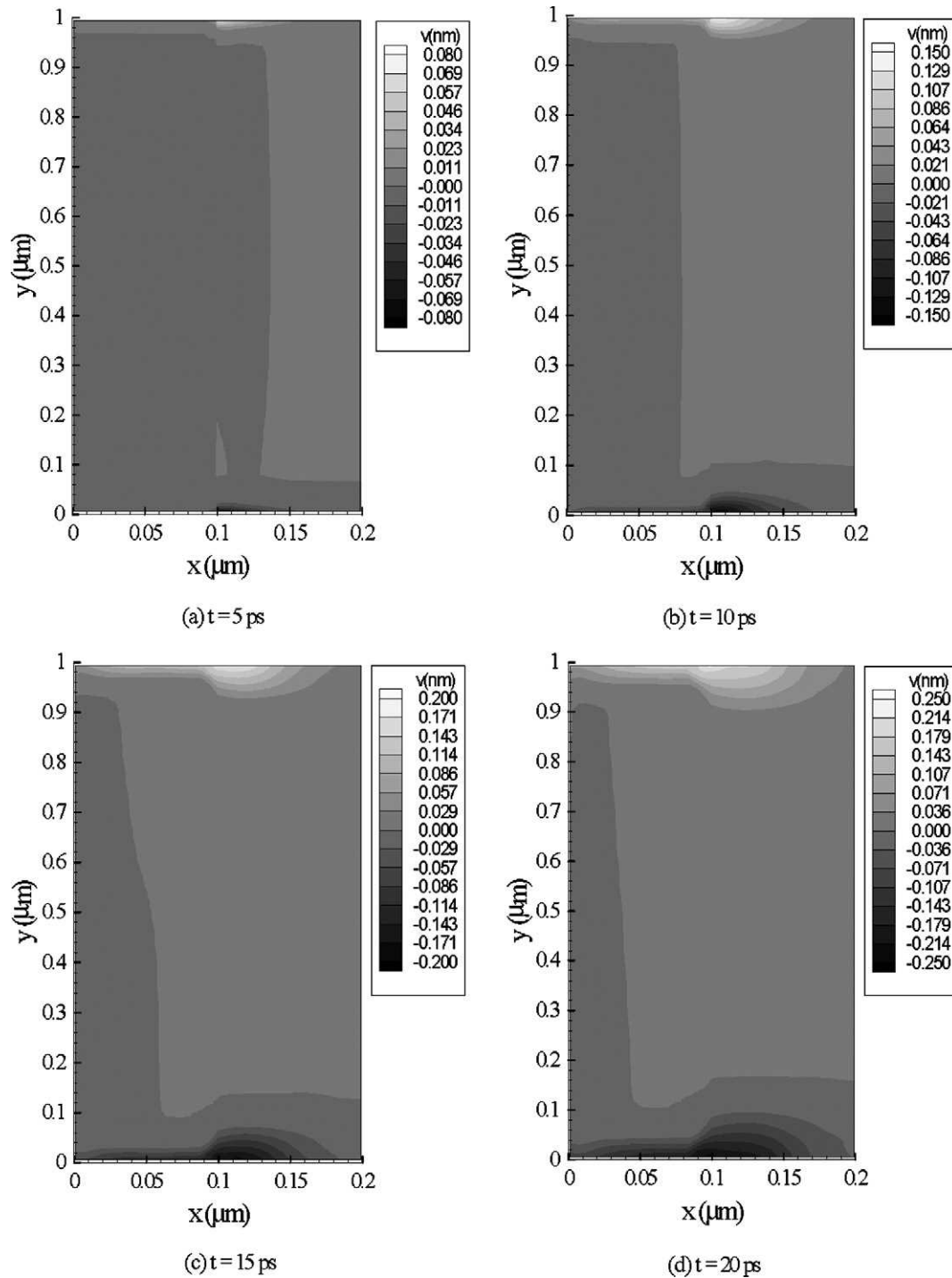


Fig. 14. Displacement ( $v$ ) profiles at different times with laser fluence  $J = 1000 \text{ J m}^{-2}$ .

mesh size had no significant effect on the solution and hence this method is only weakly dependent on the grid. Figs. 5 and 6 show respectively the comparison of electron temperature and lattice temperature along  $x$  at  $y = 0 \text{ μm}$  with three different laser fluences ( $J = 500 \text{ J m}^{-2}$ ,  $1000 \text{ J m}^{-2}$  and  $2000 \text{ J m}^{-2}$ ) at different times (a)  $t = 0.25 \text{ ps}$ , (b)  $t = 0.5 \text{ ps}$ , (c)  $t = 1 \text{ ps}$ , (d)  $t = 10 \text{ ps}$ , and (e)  $t = 20 \text{ ps}$ . It can be seen that the electron temperature rises to its maximum at the beginning and then decreases while the lattice temperature rises

gradually with time. Figs. 7 and 8 show comparison of displacement  $u$  (thickness direction) and  $v$  (length direction) along  $x$  at  $y = 0 \text{ μm}$  with three different laser fluences ( $J = 500 \text{ J m}^{-2}$ ,  $1000 \text{ J m}^{-2}$  and  $2000 \text{ J m}^{-2}$ ) at different times (a)  $t = 1 \text{ ps}$ , (b)  $t = 5 \text{ ps}$ , (c)  $t = 10 \text{ ps}$ , and (d)  $t = 20 \text{ ps}$ . Figs. 9 and 10 show comparison of normal stress  $\sigma_x$  (thickness direction) and  $\sigma_y$  (length direction) along  $x$  at  $y = 0 \text{ μm}$  with three different laser fluences ( $J = 500 \text{ J m}^{-2}$ ,  $1000 \text{ J m}^{-2}$  and  $2000 \text{ J m}^{-2}$ ) at different times (a)  $t = 1 \text{ ps}$ , (b)  $t = 5 \text{ ps}$ , (c)  $t = 10 \text{ ps}$ ,

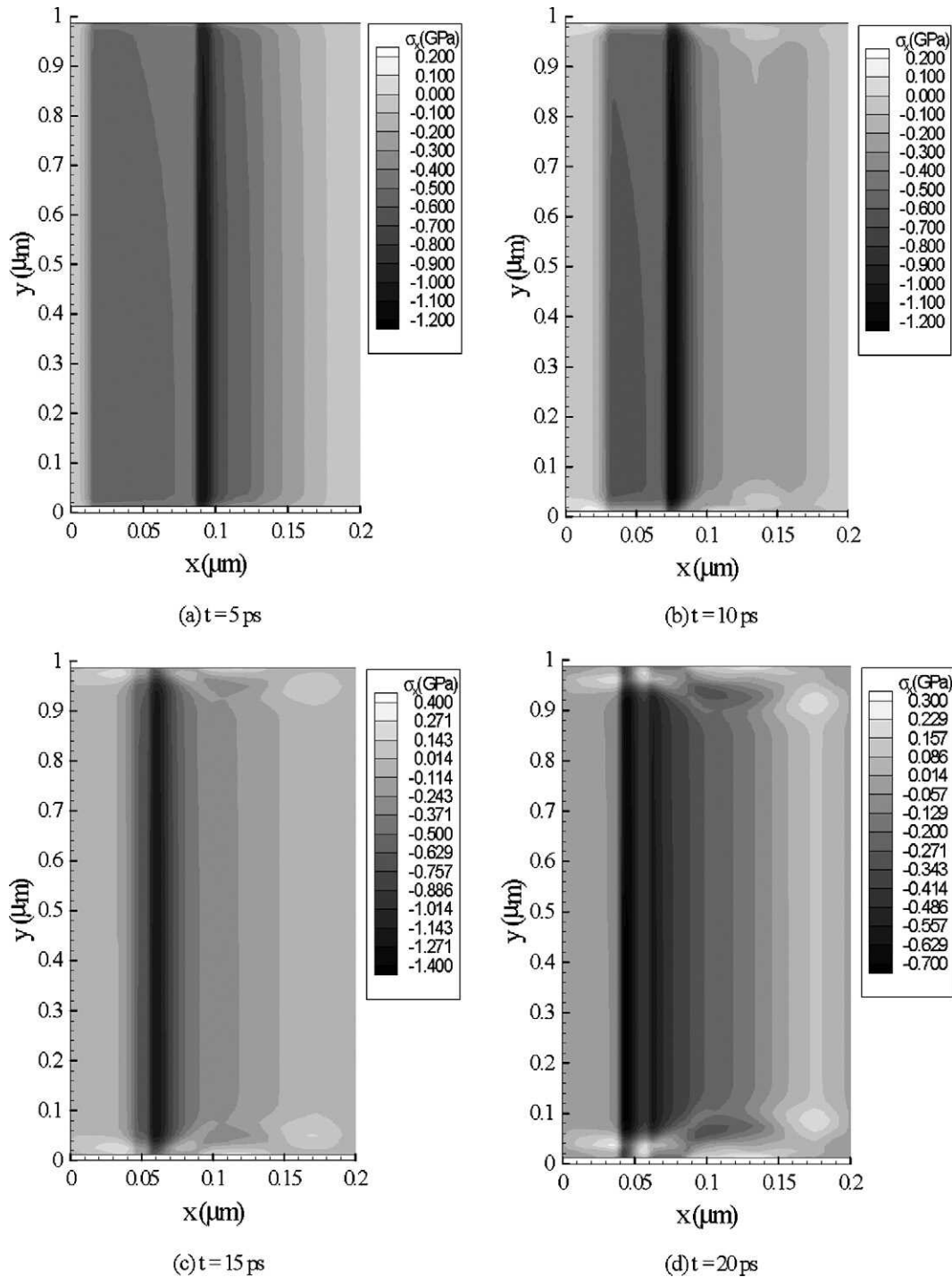


Fig. 15. Normal stress ( $\sigma_x$ ) profiles at different times with laser fluence  $J = 1000 \text{ J m}^{-2}$ .

and (d)  $t = 20 \text{ ps}$ . Figs. 11 and 12 show the contours of electron temperature profile and lattice temperature profile with the laser fluence of  $J = 1000 \text{ J m}^{-2}$  at different times (a)  $t = 0.25 \text{ ps}$ , (b)  $t = 0.5 \text{ ps}$ , (c)  $t = 1 \text{ ps}$  and (d)  $t = 10 \text{ ps}$ , respectively. Figs. 13–16 show the contours of displacement  $u$  (thickness direction) profile, displacement  $v$  (length direction) profile, normal stress  $\sigma_x$  (thickness direction) profile, and normal stress  $\sigma_y$  (length direction) profile with the laser fluence of  $J = 1000 \text{ J m}^{-2}$  at different times (a)  $t = 1 \text{ ps}$ , (b)  $t = 5 \text{ ps}$ ,

(c)  $t = 10 \text{ ps}$ , and (d)  $t = 20 \text{ ps}$ , respectively. The analysis of displacement and stress waves reveals the significance of the hot-electron blast effect on the ultrafast deformation mainly along the thickness direction. Furthermore, the proposed methodology allows us to obtain the solution free from non-physical oscillations.

To see the effect of thermal conductivity of electrons on the numerical algorithm, we chose a more general form of the electron thermal conductivity ( $k_e$ ) as follows [16,21]:

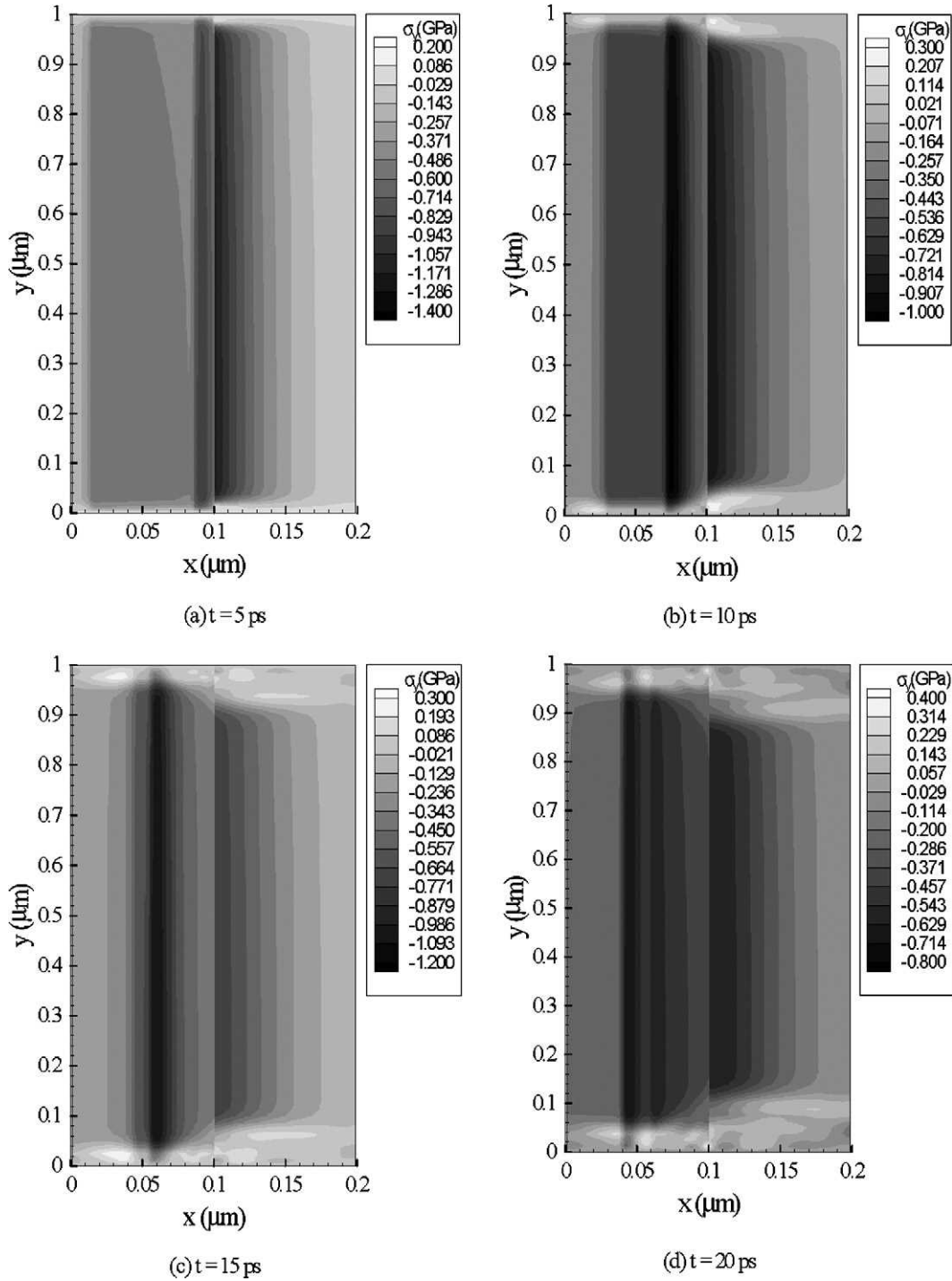


Fig. 16. Normal stress ( $\sigma_y$ ) profiles at different times with laser fluence  $J = 1000 \text{ J m}^{-2}$ .

$$k_e = \chi \frac{(\phi_e^2 + 0.16)^{5/4} (\phi_e^2 + 0.44) \phi_e}{(\phi_e^2 + 0.092)^{1/2} (\phi_e^2 + \eta \phi_l)} \quad (42)$$

where

$$\phi_e = T_e/T_F \quad \text{and} \quad \phi_l = T_l/T_F$$

are the normalized electron and lattice temperature with  $T_F$  denoting the Fermi temperature;  $\chi$  and  $\eta$  are constants. For high electron temperature  $\phi_e \gg 1$ , Eq. (42) results in the well known dependence  $k_e \sim T_e^{5/2}$ , which is characteristic for low-density

plasma. In the low electron temperature limit  $\phi_e \ll 1$ , Eq. (42) reduces to the linear equation  $k_e = k_{e0}(T_e/T_l)$ . Due to the lack of information on chromium, we only consider a single 100-nm gold film heated by laser pulse with the fluence  $J = 500 \text{ J m}^{-2}$  and  $\chi = 353 \text{ W m}^{-1} \text{ K}^{-1}$ ,  $\eta = 0.16$ ,  $T_F = 6.42 \times 10^4 \text{ K}$ . Fig. 17 shows the comparison of numerical results obtained based on Eqs. (41) and (42), respectively. It can be seen from the figure that there is no significant difference between these two.



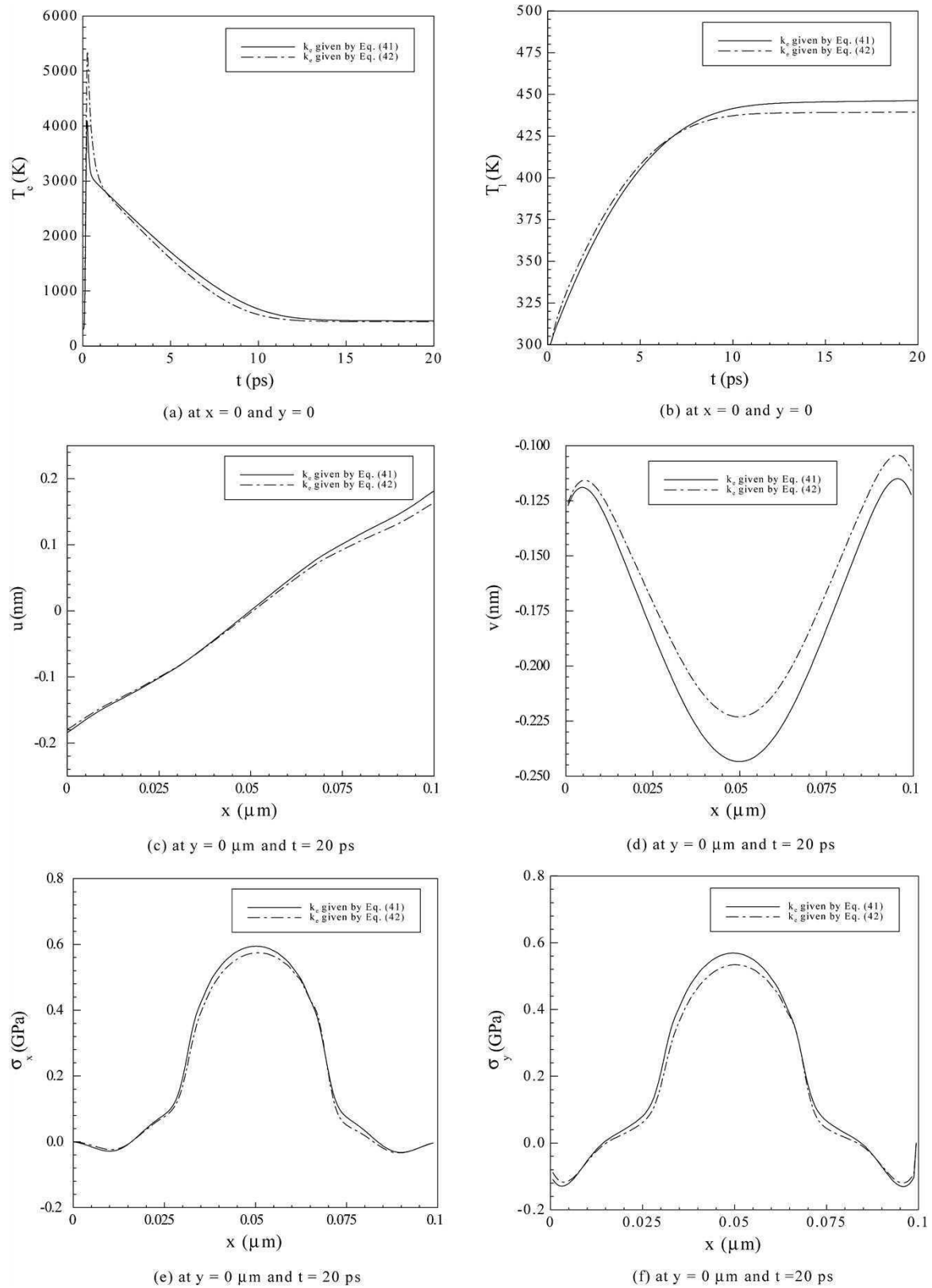


Fig. 17. Comparison of numerical results obtained based on Eqs. (41) and (42).

Table 1  
Thermophysical properties

Properties	Unit	Gold	Chromium	Others
$\rho$	$\text{kg m}^{-3}$	19300	7190	
$\Lambda$	$\text{J m}^{-3} \text{K}^{-2}$	70	193.3	
$\lambda$	Pa	$199.0 \times 10^9$	$83.3 \times 10^9$	
$\mu$	Pa	$27.0 \times 10^9$	$115.0 \times 10^9$	
$\alpha_T$	$\text{K}^{-1}$	$14.2 \times 10^{-6}$	$4.9 \times 10^{-6}$	
$C_{e0}$	$\text{J m}^{-3} \text{K}^{-1}$	$2.1 \times 10^4$	$5.8 \times 10^4$	
$C_l$	$\text{J m}^{-3} \text{K}^{-1}$	$2.5 \times 10^6$	$3.3 \times 10^6$	
$G$	$\text{W m}^{-3} \text{K}^{-1}$	$2.6 \times 10^{16}$	$42 \times 10^{16}$	
$K_e$	$\text{W m}^{-1} \text{K}^{-1}$	315	94	
$T_F$	K	$6.42 \times 10^4$		
$\chi$	$\text{W m}^{-1} \text{K}^{-1}$	353		
$\eta$		0.16		
$R$				0.93
$t_p$	s			$0.1 \times 10^{-12}$
$x_s$	m			$15.3 \times 10^{-9}$
$y_s$	m			$1 \times 10^{-6}$
$J$	$\text{J m}^{-2}$			500, 1000, 2000

## 5. Conclusion

We have developed a finite difference method for studying thermal deformation in a double-layered thin film exposed to ultrashort pulsed lasers. The method, based on the parabolic two-step heat transport equations, accounts for the coupling effect between lattice temperature and strain rate, as well as for the hot-electron blast effect in momentum transfer. By introducing the velocity components into the dynamic equations of motion, we have developed a methodology that allowed us to avoid non-physical oscillations in the solution, as illustrated by several numerical experiments.

Further research will focus on the case that the effects of acoustic and diffuse phonon mismatch across the interface are considered. The problem becomes more challenge, because such an effect will generate additional nonlinear behavior in the interfacial area.

## References

- [1] D.Y. Tzou, J.K. Chen, J.E. Beraun, Hot-electron blast induced by ultrashort-pulsed lasers in layered media, *Int. J. Heat Mass Transfer* 45 (2002) 3369–3382.
- [2] A. Mandelis, S.B. Peralta, Thermal wave based materials characterization and nondestructive evaluation of high-temperature superconductors: A critical review, in: R. Kossowsky (Ed.), *Physics and Materials Science of High Temperature Superconductors II*, Kluwer Academic, Boston, MA, 1992, pp. 413–440.
- [3] J. Opsal, The application of thermal wave technology to thickness and grain size of aluminum films, in: *Metallization: Performance and Reliability Issues for VLSI and ULSI*, vol. 1596, SPIE, 1991, pp. 120–131.
- [4] J.A. Knapp, P. Borgesen, R.A. Zuhr, Beam-solid interactions: Physical phenomena, *Mater. Res. Soc. Symp. Proc.* 157 (1990).
- [5] D.J. Elliot, B.P. Piwczyk, Single and multiple pulse ablation of polymeric and high density materials with excimer laser radiation at 193 nm and 248 nm, *Mater. Res. Soc. Symp. Proc.* 129 (1989) 627–636.
- [6] C.P. Grigoropoulos, Heat transfer in laser processing of thin films, in: C.L. Tien (Ed.), *Annual Review of Heat Transfer*, vol. V, Hemisphere, New York, 1994, pp. 77–130.
- [7] J. Narayan, V.P. Gosbole, G.W. White, Laser method for synthesis and processing of continuous diamond films on nondiamond substrates, *Science* 252 (1991) 416–418.
- [8] J.M. Hopkins, J. Sibbett, Ultrashort-pulse lasers: Big payoffs in a flash, *Sci. AM* 283 (2000) 72–79.
- [9] J. Liu, Preliminary survey on the mechanisms of the wave-like behaviors of heat transfer in living tissues, *Forschung im Ingenieurwesen* 66 (2000) 1–10.
- [10] C. Momma, S. Nolte, B.N. Chichkov, F.V. Alvensleben, A. Tunnermann, Precise laser ablation with ultrashort pulses, *App. Surf. Sci.* 109 (1997) 15–19.
- [11] M.D. Shirk, P.A. Molian, A review of ultrashort pulsed laser ablation of materials, *J. Laser Applications* 10 (1998) 18–28.
- [12] D.Y. Tzou, Ultrafast heat transport: The lagging behavior, in: 44th SPIE's Annual Meeting, 1999, July 18–22, Denver, CO.
- [13] D.Y. Tzou, Ultrafast Transient Behavior in Microscale Heat/Mass Transport, *Advanced Photon Source Millennium Lecture Series*, Argonne National Laboratories, Chicago, 2000.
- [14] D.Y. Tzou, Microscale heat transfer and fluid flow, in: 45th SPIE's Annual Meeting 2000, July 30–August 4, San Diego, CA.
- [15] S.D. Brorson, J.G. Fujimoto, E.P. Ippen, Femtosecond electron heat transfer dynamics in thin gold film, *Phys. Rev. Lett.* 59 (1987) 1962–1965.
- [16] J.K. Chen, J.E. Beraun, C.L. Tham, Comparison of one-dimensional and two-dimensional axisymmetric approaches to the thermomechanical response caused by ultrashort laser heating, *J. Opt. A: Pure Appl. Opt.* 4 (2002) 650–661.
- [17] T.Q. Qiu, C.L. Tien, Short-pulse laser heating on metals, *Int. J. Heat Mass Transfer* 35 (1992) 719–726.
- [18] Y.S. Touloukian, R.W. Powell, C.Y. Ho, P.G. Klemens, *Thermal Conductivity, Thermophysical Properties of Matter*, vol. 1, IFI/Plenum, New York, 1970.
- [19] Y.S. Touloukian, E.H. Buyco, *Specific Heat, Thermophysical Properties of Matter*, vol. 4, IFI/Plenum, New York, 1970.
- [20] T.Q. Qiu, C.L. Tien, Short-femtosecond laser heating of multi-layer metals I. Analysis, *Int. J. Heat Mass Transfer* 37 (1994) 2789–2797.
- [21] J.K. Chen, J.E. Beraun, C.L. Tham, Investigation of thermal response caused by pulse laser heating, *Numerical Heat Transfer, Part A* 44 (2003) 705–722.
- [22] J.K. Chen, J.E. Beraun, D.Y. Tzou, Thermomechanical response of metal films heated by ultrashort-pulsed lasers, *J. Thermal Stresses* 25 (2002) 539–558.